Bias reconfigurable photoresponse of infrared nanocrystal film integrated into a coupled Fabry-Perot resonator

Tung Huu Dang, Claire Abadie, Audrey Chu, Mariarosa Cavallo, Adrien Khalili, Corentin Dabard, Erwan Bossavit, Huichen Zhang, Yoann Prado, Debora Pierucci, et al.

Bias reconfigurable photoresponse of infrared nanocrystal film integrated into a coupled Fabry-Perot resonator

Tung Huu Dang[1,2], Claire Abadie[1,3], Audrey Chu[1,3], Mariarosa Cavallo[1], Adrien Khalili[1], Corentin Dabard[1], Erwan Bossavit[1], Huichen Zhang[1], Yoann Prado[1], Debora Pierucci[2], James K. Utterback[2], Yanko Todorov[2], Carlo Sirtori[2], Julien Jaeck[3], Grégory Vincent[3], Angela Vasanelli[2], Baptiste Fix[3], Emmanuel Lhuillier[1*]

[1] Sorbonne Université, CNRS, Institut des NanoSciences de Paris, INSP, F-75005 Paris, France.
[2] Laboratoire de physique de l'Ecole Normale Supérieure, ENS, Université PSL, CNRS, Sorbonne Université, Université Paris Cité, 75005 Paris, France
[3] DOTA, ONERA, Université Paris Saclay, F-91123 Palaiseau, France.

Abstract: The coupling of a photonic structure to a nanocrystal film enables light focusing over a distance compatible with the charge diffusion length. This strategy has been implemented in infrared sensors based on a nanocrystal film to maximize their absorption. Here, we demonstrate that the photonic structure can be further exploited to generate a bias-reconfigurable photoresponse. To reach this goal, we use a coupled Fabry-Perot structure that can be seen as a periodic grating with two different cavities per period. The two cavities are coupled and a resonance appears that increases the effective absorption coefficient by a factor of 30 compared to standard interdigitated electrodes. When connected in the appropriate configuration, this device enables the turning-on and -off of part of the spectral response (over a factor of 25 in magnitude) simply by tuning the applied bias (<1 V). Finally, we also demonstrate that this resonator geometry is promising for integration at the focal plane array level since the resonance is maintained for a pixel size as small as 10 µm.

Keywords: light-matter coupling, active photonics, reconfigurable response, infrared, nanocrystals.

*To whom correspondence should be sent: el@insp.upmc.fr

INTRODUCTION

Over recent years, significant efforts have been put forth to use colloidal nanocrystals (NCs) as building blocks for infrared optoelectronics. Certainly, the success achieved in the visible region, where NCs have reached a mass market as narrow emitting light down-converters, has motivated this effort. In the infrared, the prospect of bringing a cost disruption to a spectral region where detectors and sources are dramatically more expensive than their counterparts operating in the visible range has also spurred the interest in colloidal nanomaterials. Some clear successes have been obtained through the design and fabrication of components[1] such as on-chip integrated sensors[2,3], infrared cameras[4–7], spectrometer[8], and LEDs[9,10].

In addition, NCs lift the constraints of epitaxial growth. Therefore, although they still contain heavy metals (Pb and Hg mostly), low-cost/low-toxicity substrate materials can be used as opposed to epitaxially grown semiconductor thin films relying on materials such as GaAs or CdZnTe. Moreover, nanocrystals are grown at low temperatures (50 to 100°C for HgTe, below 150°C for PbS), reducing the energy consumption compared to traditional growth methods in which high temperatures (500°C and more) are commonly used. The introduction of photonic structures that focus the incident light over a thin nanocrystal layer also appears as a complementary strategy to further reduce the quantity of material per device. Aside from the advantage of minimizing the amount of heavy metal used, photonic structures have the added benefit of increasing light absorption over small distances. This is crucial since it has been established that the conduction occurs in infrared HgTe NC arrays throughout hopping between puddles of strongly coupled NCs[11], leading to small diffusion lengths. As a result, there is a strong interest in matching the device size, the carrier diffusion length[12] and the spatial extension of the electromagnetic field.

Various photonic concepts[13] have been proposed to enhance the absorption efficiency and shape the absorption spectrum: flat lenses[14], Fabry-Perot resonators, magnification of the field by metal tip[15], plasmonic cavities[3,16,17], Bragg mirrors[18], guided-mode resonators[19,20], metal-insulator-metal cavities[21], metasurfaces[22], epsilon-near-zero resonances[23,24], Helmholtz resonators[25] as well as combinations of these[26,27]. The first purpose for these photonic structures is to modify either the magnitude or the linewidth of the absorption. However, it has also been proposed that photonic structures can actively modify the shape of the spectrum[17,28] after the device is fabricated. For this, two requirements should be met: (*i*) the photonic structure needs to generate an inhomogeneous absorption map within the device, (*ii*) the charge collection needs to be electric field dependent. The last condition is an inherent property of hopping conduction[29–33]. By combining these two effects, the photocurrent will only drag the charges photogenerated in the vicinity of the electrode under low bias, whereas charge collection is possible from further away when a larger bias is applied. Since the spatial distribution of the absorption field map varies with the wavelength, one can use this effect to generate a bias-reconfigurable photoresponse. However, the magnitude of the effect reported[17,28] so far remains too weak to be used, asking for the development of alternative structures. Here, we explore the coupled Fabry-Perot[34–37] (cFP) resonator. This structure relies on two coupled Fabry-Perot resonators. Individually, each of them is designed to operate below critical coupling. However, thanks to their coupling, critical coupling condition with free-space radiation can be achieved. Beyond the anticipated strong absorption, such cFP is also promising since it may reduce the required number of periods to generate the resonance compared to the quasi-infinite grating necessary for plasmonic and guided-mode resonators[19,20]. As a result, such geometry may be compatible with a reduction of the pixel size, which is often sought-after for infrared imagers.

RESULTS AND DISCUSSION

We start by growing a semiconductor to absorb the short-wave infrared spectral range. To do so, we use colloidally prepared HgTe NCs[38,39]. The particle size is chosen so that the particles present a 2 µm cut-off wavelength after ligand exchange[11,40], see **Figure 1**a. The ligand exchange increases the inter-NC coupling and renders the film photoconductive. This procedure generally comes with a small redshift of the absorption edge, see **Figure 1**a. It is also associated with a strong reduction of the infrared absorption relative to the C-H bond resonance as the number of free ligands and the ligand length get reduced.

To design a NC based active device which spectral response can be tuned through bias application, the role of the photonic structure is to induce an inhomogeneous absorption map. In previous devices[17,28], two electromagnetic modes have been used: one, close to the electrode, will prevail under low electric field and the second, away from the electrode, will contribute to photocurrent only when the applied bias increases the diffusion length. Here, we adopt a different approach and directly design a bicolor structure where the two modes are spatially disjoint. To do so, we use a grating structure with two patterns per period, see **Figure 1**b.

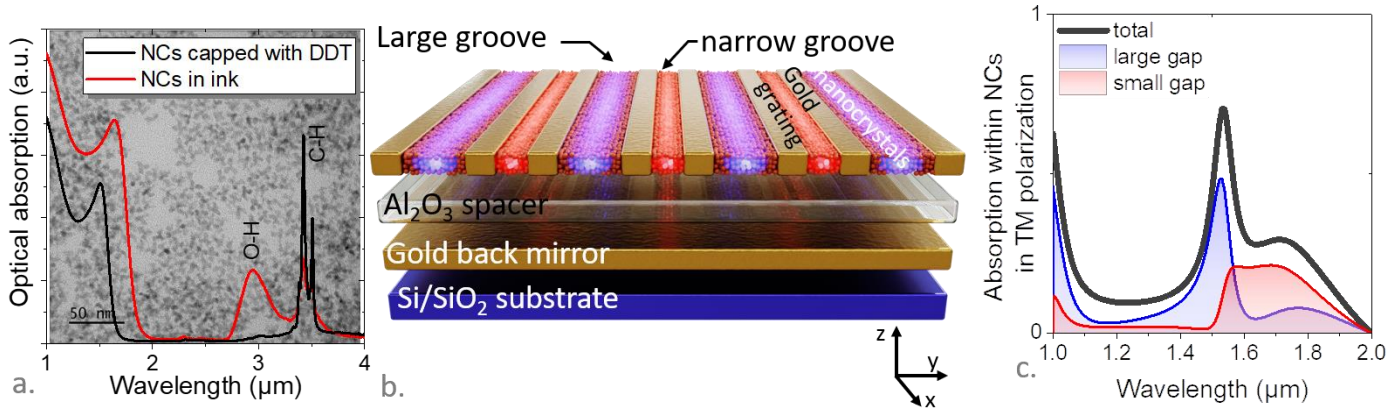

Figure 1 Coupled Fabry-Perot resonator. *a. Absorption spectra of the HgTe NCs used as infrared light absorbers, when capped with either long ligands (DDT) or short ligands (ink). b. Scheme of coupled Fabry-Perot resonators. c. Simulated absorption spectra within the NCs for the structure of part b and for the volume delimited by the small and large gaps.*

To generate a resonance that is matched with the NC band-edge, we select a 1 µm period for the grating and the openings are chosen to be 200 and 400 nm for the small and big gap structures respectively, see **Figure 1b,** S3-5 for impact of geometrical fator on the ndevice absorption spatra and Figure S5 for the details of the fabrication procedure. This structure is analog to a coupled Fabry Perot structure[34–37] in which none of cavity reaches critical coupling, which limits the associated absorption. Once the two patterns of a period are coupled within a single structure, a coupled mode is generated with a stronger absorption than the one obtained for the two individual resonators, see **Figure 1**c.

For the sake of clarity, the **Figure 1**b scheme is shown with NC only within the groove but in practice the spin coating deposition leads to the formation of quasi conformal film with NCs both in the gaps and on top of the gold digits. In the rest of the paper, we account in the simulation for the presence of the film on top of the electrodes, see Figure S1. Absorption reaches 80% for a film thickness of only 75 nm in TM polarization, corresponding to an effective absorption coefficient ≈10^5 cm^{-1}. This value is ≈30 times higher than the absorption coefficient of the HgTe NC thin film alone, which is typically around 3x10^3 cm^{-1}.

In addition, we take benefit of the field cancellation at the bottom of the structure at resonance to replace a thin layer of the structure by a transparent dielectric layer of Al_2O_3.The latter allows the grating to be used not only as a photonic structure but also as interdigitated electrodes to collect a photocurrent.

To further characterize this cFP resonator, we have coupled electromagnetic simulations with infrared scanning near-field optical microscopy (SNOM) measurements, see **Figure 2**. Experimentally, conducting the SNOM measurement on cFP coated with NCs is challenging. Thus, to mimic the nanocrystal film, we replace it with a harder dielectric thin film of Si_3N_4 whose refractive index (n_{Si3N4} =2) is comparable to the one of the NC film[41] (n_{NC}=2.35±0.1). The Si_3N_4 layer thickness has also been adjusted (140 nm) such that the main cFP resonance matches the laser source (λ=1.55 µm) of the SNOM setup, as pointed by reflectivity spectra in Figure S8.

Top views of simulated electric field maps are given in **Figure 2**b and c, respectively, in the TM and TE polarization. The simulation predicts that (*i*) the signal is polarized, with a TM polarization much more intense than the TE one and (*ii*) along the TM polarization, the signal at the main resonance (λ = 1.53µm) is mainly localized within the large gap, see **Figure 2**b and S1. Electric field maps (**Figure 2**b-c) have been simulated using the same configuration and including the 60° angle between the normal to the sample and the tip. The topography map (**Figure 2**d) shows a periodic structure presenting both large (highlighted with blue arrows) and narrow grooves (highlighted with red arrows). The experimental maps of the electric field are given in **Figure 2**e and f, respectively, in TM and TE polarization. As predicted (**Figure 2**b-c), the magnitude of the field is much weaker along the TE polarization. We can correlate the maximum field magnitude with the location of the large grooves.

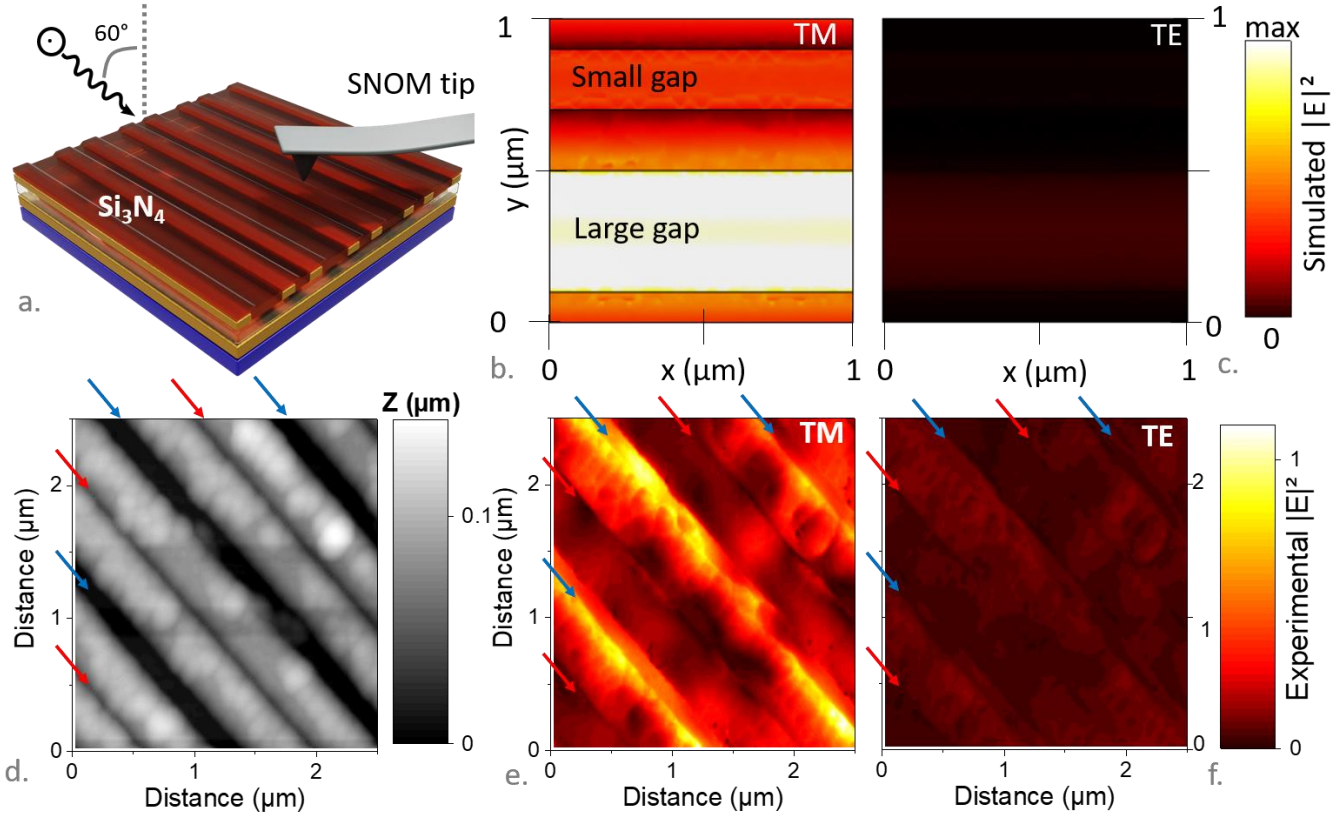

Figure 2 Infrared near-field microscopy characterization of coupled Fabry-Perot structure. *a. Schematic of the SNOM measurements on a coupled Fabry-Perot structure in which the NC layer is replaced by a thin Si_3N_4 film. The incident light comes with a 60° angle. Simulated square of the electric field map at 1.55 µm in TM (b.) and TE (c.) polarization. d. Topography map of the coupled*

Fabry-Perot structure. Blue and red arrows highlight, respectively, the localization of the large and small gaps. Experimental square of the electric field map at 1.55 µm in TM (e.) and TE (f.) polarization, obtained from the third order demodulation of the SNOM signal.

Now that the optical behavior of the cFP is established, we can focus on its photoconductive properties. The charge collection is determined by the way the grating is used as electrode. Various configurations can be implemented, see **Figure 3**a-b. Here we focus on two of them: the 'interdigitated" configuration (**Figure 3**a and S9), in which two consecutive digits are connected to opposite electrodes, and the "tuning fork" configuration (**Figure 3**b and S10-11), where the small grooves separate digits connected to the same electrode. In the tuning fork configuration, the electrostatic field resulting from bias application is only applied over the large gap, whereas in the interdigitated configuration, the electrostatic field is applied over both the large and narrow gaps.

The photocurrent spectra obtained using the tuning fork configuration depict a single resonance with a very weak bias dependence, see **Figure 3**d and S10. On the other hand, the photocurrent spectrum of the interdigitated configuration can significantly be tuned with bias.

In the interdigitated configuration, under low bias, we only observe one peak whose energy matches the main resonance of the cFP. Once a stronger electric field is applied, a second contribution at lower energy appears in the spectrum, see **Figure 3**c. The bias dependence of the cFP can be rationalized as follows: since the absorption is stronger in the larger gap (**Figure 1**c), the photocurrent from the large gap prevails at low electric fields. When the bias is increased, the electrostatic field gets more important over the narrow gap, which is twice as small, and charges generated in the narrow gap are more effectively collected.[11,12,29,42] As a result, the higher the field, the more efficiently the narrow gap contributes to the photocurrent. This effect combines not only the higher magnitude of the electric field in the narrow gap but also the more efficient hopping conduction at short distance. In other words, the bias is used to tune the ratio of the photocurrent signals generated within the two Fabry-Perot cavities. This interpretation is consistent with the lack of bias dependency of the response in the tuning fork configuration, which collects solely the photocurrent generated within the large gap. A small shift can be noticed between the spectra of the tuning fork and the large gap contribution of the interdigitated configuration. This can be fully correlated to NC film thickness determined by profilometry, see Figure S2.

Using the cFP structure, it is possible to turn-on and -off the photocurrent in the 1.6 to 1.9 µm range with the bias as a control knob, see the inset of **Figure 3**c. The magnitude of the modulation reaches a factor of 25, which is far more than the previously reported bias-induced spectrum modifications[17,28] that only modified the magnitude of the signal without affecting the spectral shape[43–46]. Compared with Stark modulation, the bias reconfigurability of the cFP structure also enables operation under a strongly reduced electric field since it has been predicted that, in HgTe NC arrays, electric fields above 100 $kV.cm^{-1}$ are required to obtain a shift of only 30 nm[17]. Here, fields 10 times lower can displace the response by more than 250 nm. It is worth mentioning that the bias required to generate the effect is compatible with the typical bias applied by a CMOS read-out circuit (3 V typically).

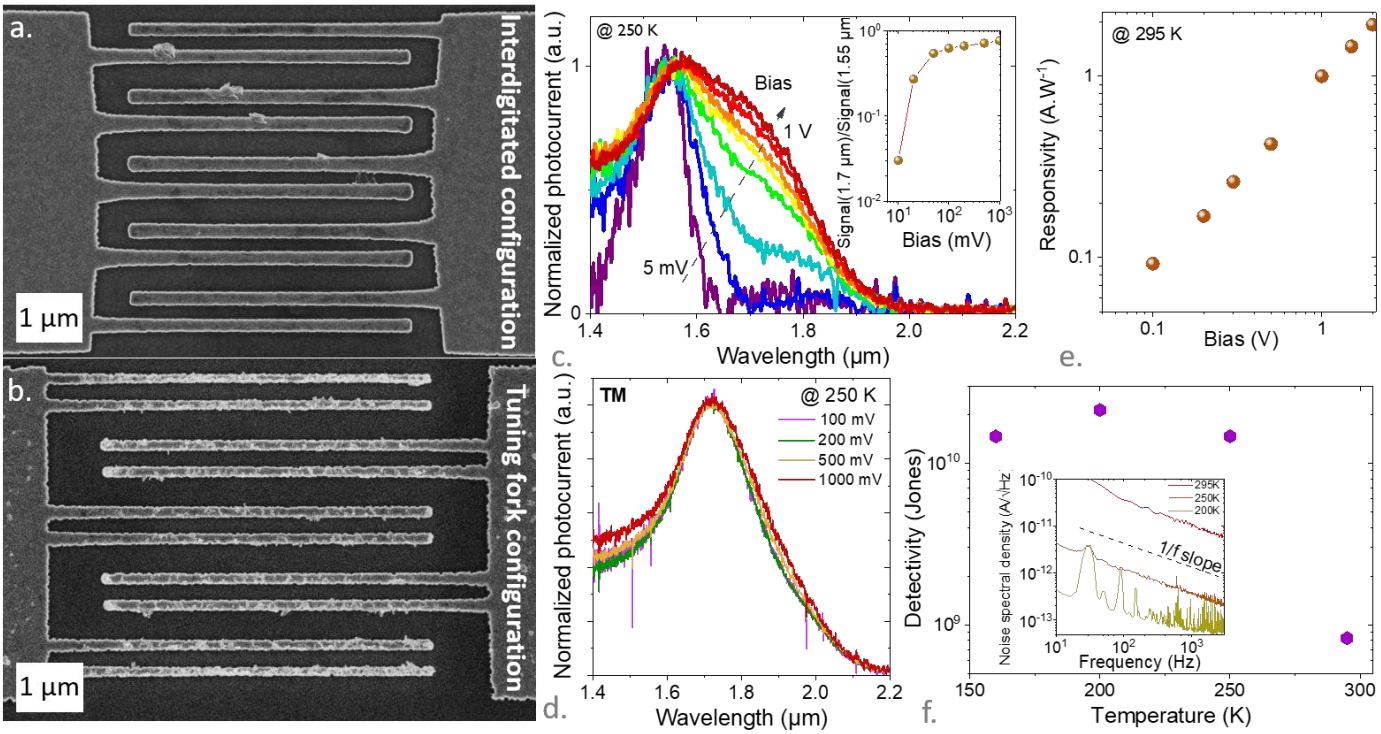

Figure 3 Bias reconfigurable photoresponse. *Scanning electron microscopy image of coupled Fabry-Perot structure connected using interdigitated (a.) or tuning fork (b.) configuration. c. Unpolarized photocurrent spectra under various biases in the interdigitated configuration, measured at 250 K. The inset shows the bias dependence of the ratio of intensities between the signal at 1.7 µm and the one at 1.5 µm. d. Photocurrent spectra under various biases in the tuning fork configuration, measured at 250 K. e. Responsivity under illumination from a black body at 980°C (i.e., broadband) as a function of the applied bias, measured at 295 K. f. Specific detectivity as a function of the device temperature, measured at 1 V and 1 kHz. The inset shows the noise current spectral density as a function of the signal frequency, measured at three different temperatures.*

As an infrared photodetector, the cFP structure can lead to a responsivity as high as 2 A.W^{-1} under broadband blackbody illumination, see **Figure 3**e. This corresponds to an external quantum efficiency of around 120%, suggesting the presence of photoconductive gain[47]. The latter is favored by the short interelectrode spacing[12], since the gain scales as $\frac{\tau_{carrier}}{\tau_{transit}}$ with $\tau_{carrier}$the photocarrier lifetime and $\tau_{transit}$ the transit time, *i.e.* the duration for the carrier to go across the channel. A shorter electrode spacing allows a faster crossing and thus magnifies the gain. The noise in the structure remains limited by *1/f* contribution[48,49], see the inset of **Figure 3**f, which currently limits the specific detectivity of the structure to 2x10^{10} jones when operating at 200 K. This value is typically higher than the one reported for photoconductive geometries that do not implement a light management strategy, but it still remains smaller than the one of state-of-the-art devices based on the same material at the same wavelength, see table S1. Conversely, the cFP structure is the one presenting the strongest spectral reconfigurability.

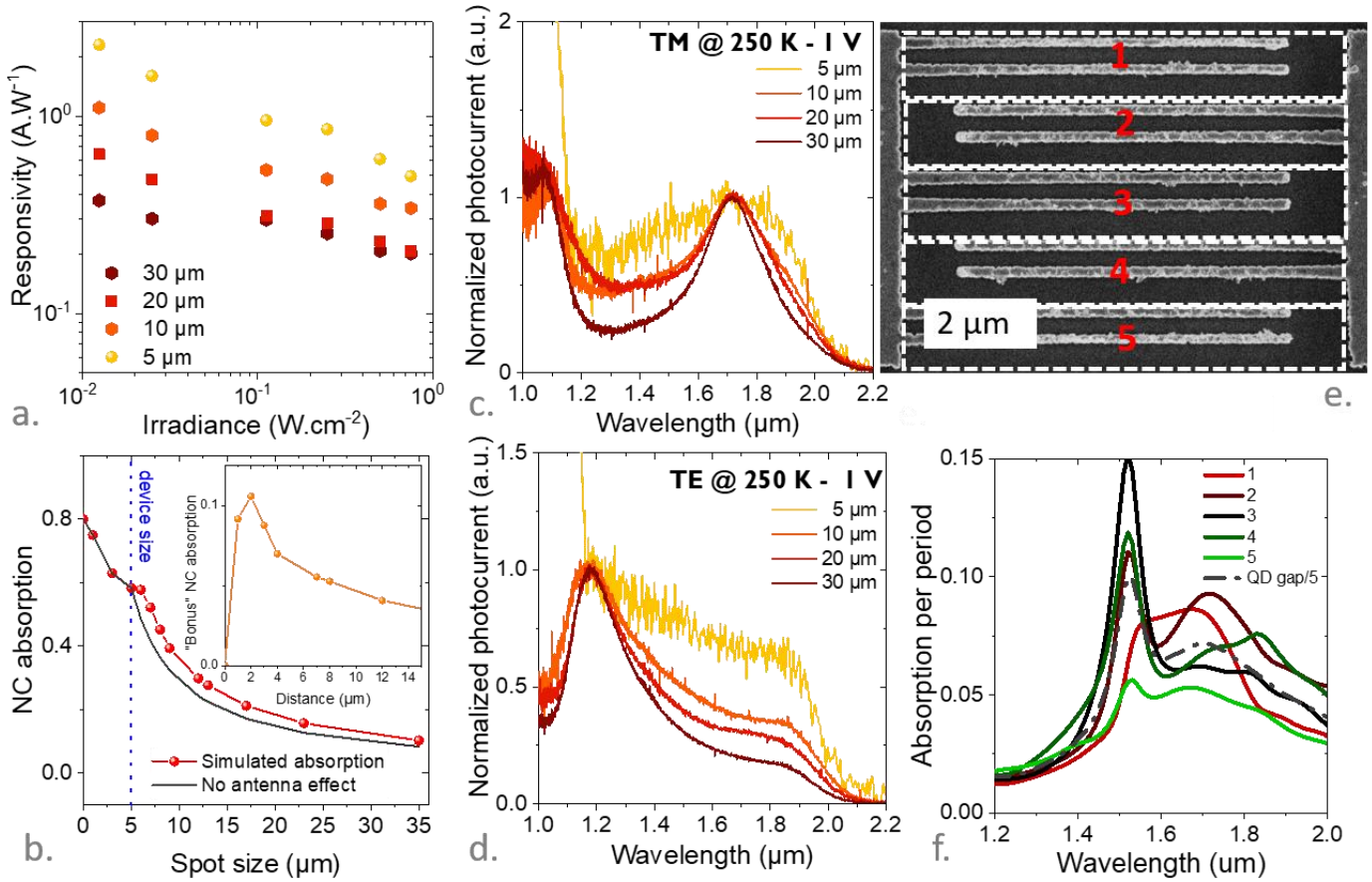

Figure 4 Antenna effect and potential for small pixel design*. a. Responsivity as a function of the incident irradiance under 1V, measured at 295 K, for several device sizes. b. Simulated Absorption in NC layer as the illumination spot size increases. The inset shows the NC absorption gained due to the antenna effect as a function of distance to the grating area. c. Normalized photocurrent spectra under 1V, along TM polarization for various pixel sizes. d. Normalized photocurrent spectra under 1V, along TE polarization for various pixel sizes. e. Scanning electron microscopy image of the coupled Fabry-Perot structure with 5 periods. f. Simulated absorption spectra for each period of the device are depicted in part (e.) The dashed line is the average absorption*

By changing the number of periods of the grating and the electrode length, we also have investigated the impact of the device size (*i.e*. size of the grating) on the device response, see **Figure 4** and S7. We notice that smaller devices present a larger responsivity, see **Figure 4**a. This suggests a possible antenna effect that enables photon collection outside of the cFP structure. In **Figure 4**b, we have simulated absorption in the NC layer with different sizes of the illumination spot for a 5-period cFP (*i.e.,* the structure size of 5 µm). **Figure 4**b compares our simulated NC absorption with the theoretical NC absorption *in the absence of* antenna effect (*i.e.,* the structure only absorbs radiation impinging on its physical area). When the spot size is larger than the device's physical size, the cFP structure shows a stronger absorption than the one obtained without antenna effect, implying photon collection outside the grating area. The difference in absorption with and without antenna effect is presented as a function of the distance to the device in the inset of **Figure 4**b and presents a maximum at around 2 µm, which is very close to the resonance wavelength of the cFP device. In other words, the cFP can collect photons 2 µm away from the grating, it is thus of high interest to shrink the device size to maximize the benefit of this "free" absorption, by reducing at the same time the noise.[50] In **Figure 4**c and d, we have measured the photocurrent spectra for various device sizes while electrodes are connected in the tuning fork configuration. The characteristic resonance of the cFP along the TM polarization is well observed for pixel size down to 10 µm. This

suggests that this geometry of the resonator might be compatible with the next generation of imagers in the short-wave infrared in which pixel size below 10 µm will be targeted. However, a structure only including 5 periods (5 µm size) does not present the cFP resonance. Simulation (**Figure 4**f) clearly shows that the external periods of the structure that are only coupled to a single Fabry-Perot on one side presents a reduced absorption. This observation certainly sets the smallest dimension the cFP structure can be realized.

Conclusion

To summarize, we have described a new type of resonator that can increase the absorption of an infrared NC film. The cFP structure comprises a grating with two patterns per period. It leads to an effective increase of the absorption coefficient by a factor of almost 30 in the TM polarization, reaching now a value of approximately 10^5 cm^{-1}. Beyond the enhanced absorption, the cFP device enables the design of a bias-reconfigurable photoresponse. The photocurrent signal over a 300 nm spectral region can be turned on and off by a factor of 25 by using only low driving voltage (<1 V, which is fully compatible with CMOS read-out circuits). Beyond the benefit of bringing NC as an active medium for nanophotonics, such reconfigurability of the response is interesting to generate band rejection filtering, which could prevent blurriness of the sensor by countermeasures. In addition, the cFP device presents an antenna effect and enables photon collection from outside the structure over a distance that matches the resonance wavelength in the structure. cFP also shows great potential for being transferred at the imager level since it does not require an infinite grating to be effective, and resonance is observed for pixel sizes as small as 10 µm.

Supporting Information

Supporting Information include (*i*) method for nanocrystal synthesis, (*ii*) electromagnetic design, fabrication procedure and near field microscopy of the cFP structure (*iii*) additional photocurrent spectra as a function of bias and temperature and (*iv*) comparison with state-of-the-art device based on nanocrystal film coupled to photonic structure.

COMPETING INTEREST

The authors declare no competing financial interests.

FUNDING SOURCES

The project is supported by ERC grant blackQD (grant n° 756225) and AQDtive (grant n° 101086358). We acknowledge the use of clean-room facilities from the “Centrale de Proximité Paris-Centre”. This work was supported by French state funds managed by the ANR more specifically within the grants IPER-Nano2 (ANR-18-CE30-0023), Copin (ANR-19-CE24-0022), Frontal (ANR-19-CE09-0017), Graskop (ANR-19-CE09-0026), NITQuantum (ANR-20-ASTR-0008-01), Bright (ANR-21-CE24-0012-02), MixDferro (ANR-21-CE09-0029) and Quicktera (ANR-22-CE09-0018).

REFERENCES

(1) Kershaw, S. V.; Rogach, A. L. Infrared Emitting HgTe Quantum Dots and Their Waveguide and Optoelectronic Devices. *Z. Für Phys. Chem.* **2015**, *229* (1–2), 23–64. https://doi.org/10.1515/zpch-2014-0590.

(2) Tang, X.; Chen, M.; Kamath, A.; Ackerman, M. M.; Guyot-Sionnest, P. Colloidal Quantum-Dots/Graphene/Silicon Dual-Channel Detection of Visible Light and Short-Wave Infrared. *ACS Photonics* **2020**, *7* (5), 1117–1121. https://doi.org/10.1021/acsphotonics.0c00247.
(3) Zhu, B.; Chen, M.; Zhu, Q.; Zhou, G.; Abdelazim, N. M.; Zhou, W.; Kershaw, S. V.; Rogach, A. L.; Zhao, N.; Tsang, H. K. Integrated Plasmonic Infrared Photodetector Based on Colloidal HgTe Quantum Dots. *Adv. Mater. Technol.* **2019**, *4* (10), 1900354.
(4) Gréboval, C.; Darson, D.; Parahyba, V.; Alchaar, R.; Abadie, C.; Noguier, V.; Ferré, S.; Izquierdo, E.; Khalili, A.; Prado, Y.; Potet, P.; Lhuillier, E. Photoconductive Focal Plane Array Based on HgTe Quantum Dots for Fast and Cost-Effective Short-Wave Infrared Imaging. *Nanoscale* **2022**, *14* (26), 9359–9368. https://doi.org/10.1039/D2NR01313D.
(5) Zhang, S.; Bi, C.; Qin, T.; Liu, Y.; Cao, J.; Song, J.; Huo, Y.; Chen, M.; Hao, Q.; Tang, X. Wafer-Scale Fabrication of CMOS-Compatible Trapping-Mode Infrared Imagers with Colloidal Quantum Dots. *ACS Photonics* **2023**, *10* (3), 673–682. https://doi.org/10.1021/acsphotonics.2c01699.
(6) Zhang, S.; Bi, C.; Tan, Y.; Luo, Y.; Liu, Y.; Cao, J.; Chen, M.; Hao, Q.; Tang, X. Direct Optical Lithography Enabled Multispectral Colloidal Quantum-Dot Imagers from Ultraviolet to Short-Wave Infrared. *ACS Nano* **2022**, *16* (11), 18822–18829. https://doi.org/10.1021/acsnano.2c07586.
(7) Zhang, H.; Alchaar, R.; Prado, Y.; Khalili, A.; Gréboval, C.; Cavallo, M.; Bossavit, E.; Dabard, C.; Dang, T. H.; Abadie, C.; Methivier, C.; Darson, D.; Parahyba, V.; Potet, P.; Ramade, J.; Silly, M. G.; Utterback, J. K.; Pierucci, D.; Ithurria, S.; Lhuillier, E. Material Perspective on HgTe Nanocrystal-Based Short-Wave Infrared Focal Plane Arrays. *Chem. Mater.* **2022**, *34* (24), 10964–10972. https://doi.org/10.1021/acs.chemmater.2c02955.
(8) Grotevent, M. J.; Yakunin, S.; Bachmann, D.; Romero, C.; Vázquez de Aldana, J. R.; Madi, M.; Calame, M.; Kovalenko, M. V.; Shorubalko, I. Integrated Photodetectors for Compact Fourier-Transform Waveguide Spectrometers. *Nat. Photonics* **2022**.
(9) Shen, X.; Peterson, J. C.; Guyot-Sionnest, P. Mid-Infrared HgTe Colloidal Quantum Dot LEDs. *ACS Nano* **2022**, *16* (5), 7301–7308. https://doi.org/10.1021/acsnano.2c01694.
(10) Qu, J.; Weis, M.; Izquierdo, E.; Mizrahi, S. G.; Chu, A.; Dabard, C.; Gréboval, C.; Bossavit, E.; Prado, Y.; Péronne, E.; Ithurria, S.; Patriarche, G.; Silly, M. G.; Vincent, G.; Boschetto, D.; Lhuillier, E. Electroluminescence from Nanocrystals above 2 Mm. *Nat. Photonics* **2022**, *16* (1), 38–44. https://doi.org/10.1038/s41566-021-00902-y.
(11) Lan, X.; Chen, M.; Hudson, M. H.; Kamysbayev, V.; Wang, Y.; Guyot-Sionnest, P.; Talapin, D. V. Quantum Dot Solids Showing State-Resolved Band-like Transport. *Nat. Mater.* **2020**, *19* (3), 323–329. https://doi.org/10.1038/s41563-019-0582-2.
(12) Chu, A.; Gréboval, C.; Prado, Y.; Majjad, H.; Delerue, C.; Dayen, J.-F.; Vincent, G.; Lhuillier, E. Infrared Photoconduction at the Diffusion Length Limit in HgTe Nanocrystal Arrays. *Nat. Commun.* **2021**, *12* (1), 1794.
(13) Chen, M.; Lu, L.; Yu, H.; Li, C.; Zhao, N. Integration of Colloidal Quantum Dots with Photonic Structures for Optoelectronic and Optical Devices. *Adv. Sci.* **2021**, *8* (18), 2101560. https://doi.org/10.1002/advs.202101560.
(14) Ning, Y.; Zhang, S.; Hu, Y.; Hao, Q.; Tang, X. Simulation of Monolithically Integrated Meta-Lens with Colloidal Quantum Dot Infrared Detectors for Enhanced Absorption. *Coatings* **2020**, *10*, 1218.
(15) Chen, M.; Shao, L.; Kershaw, S. V.; Yu, H.; Wang, J.; Rogach, A. L.; Zhao, N. Photocurrent Enhancement of HgTe Quantum Dot Photodiodes by Plasmonic Gold Nanorod Structures. *ACS Nano* **2014**, *8* (8), 8208–8216.
(16) Yifat, Y.; Ackerman, M.; Guyot-Sionnest, P. Mid-IR Colloidal Quantum Dot Detectors Enhanced by Optical Nano-Antennas. *Appl. Phys. Lett.* **2017**, *110* (4), 041106. https://doi.org/10.1063/1.4975058.
(17) Dang, T. H.; Vasanelli, A.; Todorov, Y.; Sirtori, C.; Prado, Y.; Chu, A.; Gréboval, C.; Khalili, A.; Cruguel, H.; Delerue, C.; Vincent, G.; Lhuillier, E. Bias Tunable Spectral Response of Nanocrystal Array in a Plasmonic Cavity. *Nano Lett.* **2021**, *21* (15), 6671–6677.
(18) Tang, X.; Ackerman, M. M.; Guyot-Sionnest, P. Acquisition of Hyperspectral Data with Colloidal Quantum Dots. *Laser Photonics Rev.* **2019**, *13*, 1900165.
(19) Chu, A.; Gréboval, C.; Goubet, N.; Martinez, B.; Livache, C.; Qu, J.; Rastogi, P.; Bresciani, F. A.; Prado, Y.; Suffit, S.; Ithurria, S.; Vincent, G.; Lhuillier, E. Near Unity Absorption in Nanocrystal Based Short Wave Infrared Photodetectors Using Guided Mode Resonators. *ACS Photonics* **2019**, *6* (10), 2553–2561.
(20) Gréboval, C.; Chu, A.; Magalhaes, D. V.; Ramade, J.; Qu, J.; Rastogi, P.; Khalili, A.; Chee, S.-S.; Aubin, H.; Vincent, G.; Bals, S.; Delerue, C.; Lhuillier, E. Ferroelectric Gating of Narrow Band-Gap Nanocrystal

Arrays with Enhanced Light–Matter Coupling. *ACS Photonics* **2021**, *8* (1), 259–268. https://doi.org/10.1021/acsphotonics.0c01464.
(21) Dhawan, A. R.; Nasilowski, M.; Wang, Z.; Dubertret, B.; Maître, A. Fabrication of Efficient Single-Emitter Plasmonic Patch Antennas by Deterministic In Situ Optical Lithography Using Spatially Modulated Light. *Adv. Mater.* **2022**, *34* (11), 2108120. https://doi.org/10.1002/adma.202108120.
(22) Đorđević, N.; Schwanninger, R.; Yarema, M.; Koepfli, S.; Yarema, O.; Salamin, Y.; Lassaline, N.; Cheng, B.; Yazdani, N.; Dorodnyy, A.; Fedoryshyn, Y. M.; Wood, V.; Leuthold, J. Metasurface Colloidal Quantum Dot Photodetectors. *ACS Photonics* **2022**, *9* (2), 482–492. https://doi.org/10.1021/acsphotonics.1c01204.
(23) Caligiuri, V.; Palei, M.; Biffi, G.; Artyukhin, S.; Krahne, R. A Semi-Classical View on Epsilon-Near-Zero Resonant Tunneling Modes in Metal/Insulator/Metal Nanocavities. *Nano Lett.* **2019**, *19* (5), 3151–3160. https://doi.org/10.1021/acs.nanolett.9b00564.
(24) Caligiuri, V.; Palei, M.; Imran, M.; Manna, L.; Krahne, R. Planar Double-Epsilon-Near-Zero Cavities for Spontaneous Emission and Purcell Effect Enhancement. *ACS Photonics* **2018**, *5* (6), 2287–2294. https://doi.org/10.1021/acsphotonics.8b00121.
(25) Abadie, C.; Paggi, L.; Fabas, A.; Khalili, A.; Dang, T. H.; Dabard, C.; Cavallo, M.; Alchaar, R.; Zhang, H.; Prado, Y.; Bardou, N.; Dupuis, C.; Xu, X. Z.; Ithurria, S.; Pierucci, D.; Utterback, J. K.; Fix, B.; Vincent, G.; Bouchon, P.; Lhuillier, E. Helmholtz Resonator Applied to Nanocrystal-Based Infrared Sensing. *Nano Lett.* **2022**, *22* (21), 8779–8785.
(26) Dang, T. H.; Abadie, C.; Khalili, A.; Gréboval, C.; Zhang, H.; Prado, Y.; Xu, X. Z.; Gacemi, D.; Descamps-Mandine, A.; Ithurria, S.; Todorov, Y.; Sirtori, C.; Vasanelli, A.; Lhuillier, E. Broadband Enhancement of Mid-Wave Infrared Absorption in a Multi-Resonant Nanocrystal-Based Device. *Adv. Opt. Mater.* **2022**, *10* (9), 2200297. https://doi.org/10.1002/adom.202200297.
(27) Tang, X.; Ackerman, M. M.; Guyot-Sionnest, P. Thermal Imaging with Plasmon Resonance Enhanced HgTe Colloidal Quantum Dot Photovoltaic Devices. *ACS Nano* **2018**, *12* (7), 7362–7370.
(28) Dang, T. H.; Khalili, A.; Abadie, C.; Gréboval, C.; Cavallo, M.; Zhang, H.; Bossavit, E.; Utterback, J. K.; Dandeu, E.; Prado, Y.; Vincent, G.; Ithurria, S.; Todorov, Y.; Sirtori, C.; Vasanelli, A.; Lhuillier, E. Nanocrystal-Based Active Photonics Device through Spatial Design of Light-Matter Coupling. *ACS Photonics* **2022**, *9* (7), 2528–2535. https://doi.org/10.1021/acsphotonics.2c00738.
(29) Xing, Y.; Yazdani, N.; Lin, W. M. M.; Yarema, M.; Zahn, R.; Wood, V. Effect of Positional Disorders on Charge Transport in Nanocrystal Quantum Dot Thin Films. *ACS Appl. Electron. Mater.* **2022**, *4* (2), 631–642. https://doi.org/10.1021/acsaelm.1c01011.
(30) Nenashev, A. V.; Jansson, F.; Baranovskii, S. D.; Österbacka, R.; Dvurechenskii, A. V.; Gebhard, F. Effect of Electric Field on Diffusion in Disordered Materials. I. One-Dimensional Hopping Transport. *Phys. Rev. B* **2010**, *81* (11), 115203. https://doi.org/10.1103/PhysRevB.81.115203.
(31) Nenashev, A. V.; Jansson, F.; Baranovskii, S. D.; Österbacka, R.; Dvurechenskii, A. V.; Gebhard, F. Effect of Electric Field on Diffusion in Disordered Materials. II. Two- and Three-Dimensional Hopping Transport. *Phys. Rev. B* **2010**, *81* (11), 115204. https://doi.org/10.1103/PhysRevB.81.115204.
(32) Richert, R.; Pautmeier, L.; Bässler, H. Diffusion and Drift of Charge Carriers in a Random Potential: Deviation from Einstein's Law. *Phys. Rev. Lett.* **1989**, *63* (5), 547–550. https://doi.org/10.1103/PhysRevLett.63.547.
(33) Arkhipov, V. I.; Bässler, H. A Model of Weak-Field Quasi-Equilibrium Hopping Transport in Disordered Materials. *Philos. Mag. Lett.* **1993**, *67* (5), 343–349. https://doi.org/10.1080/09500839308241271.
(34) Fix, B.; Jaeck, J.; Bouchon, P.; Héron, S.; Vest, B.; Haïdar, R. High-Quality-Factor Double Fabry–Perot Plasmonic Nanoresonator. *Opt. Lett.* **2017**, *42* (24), 5062. https://doi.org/10.1364/OL.42.005062.
(35) Fix, B.; Jaeck, J.; Bouchon, P.; Bardou, N.; Vest, B.; Haidar, R. Dark-Modes Excitation in Coupled Nano Fabry-Perot Structure Induced by Symmetry Breaking. **2020**. https://doi.org/10.48550/ARXIV.2011.05242.
(36) Matthia, T.; Fix, B.; Soun, L.; Dupuis, C.; Bardou, N.; Bouchon, P. High-Efficiency Second-Harmonic Generation in Coupled Nano Fabry–Perot Thin Resonators. *Opt. Lett.* **2022**, *47* (17), 4415. https://doi.org/10.1364/OL.465602.
(37) Guo, L.; Sun, Z. Cooperative Optical Trapping in Asymmetric Plasmon Nanocavity Arrays. *Opt. Express* **2015**, *23* (24), 31324–31333. https://doi.org/10.1364/OE.23.031324.
(38) Gréboval, C.; Chu, A.; Goubet, N.; Livache, C.; Ithurria, S.; Lhuillier, E. Mercury Chalcogenide Quantum Dots: Material Perspective for Device Integration. *Chem. Rev.* **2021**, *121* (7), 3627–3700. https://doi.org/10.1021/acs.chemrev.0c01120.

(39) Keuleyan, S.; Lhuillier, E.; Guyot-Sionnest, P. Synthesis of Colloidal HgTe Quantum Dots for Narrow Mid-IR Emission and Detection. *J. Am. Chem. Soc.* **2011**, *133* (41), 16422–16424. https://doi.org/10.1021/ja2079509.
(40) Martinez, B.; Ramade, J.; Livache, C.; Goubet, N.; Chu, A.; Gréboval, C.; Qu, J.; Watkins, W. L.; Becerra, L.; Dandeu, E.; Fave, J. L.; Méthivier, C.; Lacaze, E.; Lhuillier, E. HgTe Nanocrystal Inks for Extended Short-Wave Infrared Detection. *Adv. Opt. Mater.* **2019**, *7* (15), 1900348. https://doi.org/10.1002/adom.201900348.
(41) Rastogi, P.; Chu, A.; Dang, T. H.; Prado, Y.; Gréboval, C.; Qu, J.; Dabard, C.; Khalili, A.; Dandeu, E.; Fix, B.; Xu, X. Z.; Ithurria, S.; Vincent, G.; Gallas, B.; Lhuillier, E. Complex Optical Index of HgTe Nanocrystal Infrared Thin Films and Its Use for Short Wave Infrared Photodiode Design. *Adv. Opt. Mater.* **2021**, *9* (10), 2002066. https://doi.org/10.1002/adom.202002066.
(42) Nenashev, A. V.; Oelerich, J. O.; Dvurechenskii, A. V.; Gebhard, F.; Baranovskii, S. D. Fundamental Characteristic Length Scale for the Field Dependence of Hopping Charge Transport in Disordered Organic Semiconductors. *Phys. Rev. B* **2017**, *96* (3), 035204. https://doi.org/10.1103/PhysRevB.96.035204.
(43) Efros, A. L.; Delehanty, J. B.; Huston, A. L.; Medintz, I. L.; Barbic, M.; Harris, T. D. Evaluating the Potential of Using Quantum Dots for Monitoring Electrical Signals in Neurons. *Nat. Nanotechnol.* **2018**, *13* (4), 278–288. https://doi.org/10.1038/s41565-018-0107-1.
(44) Rowland, C. E.; Susumu, K.; Stewart, M. H.; Oh, E.; Mäkinen, A. J.; O'Shaughnessy, T. J.; Kushto, G.; Wolak, M. A.; Erickson, J. S.; L. Efros, A.; Huston, A. L.; Delehanty, J. B. Electric Field Modulation of Semiconductor Quantum Dot Photoluminescence: Insights Into the Design of Robust Voltage-Sensitive Cellular Imaging Probes. *Nano Lett.* **2015**, *15* (10), 6848–6854. https://doi.org/10.1021/acs.nanolett.5b02725.
(45) Scott, R.; Achtstein, A. W.; Prudnikau, A. V.; Antanovich, A.; Siebbeles, L. D. A.; Artemyev, M.; Woggon, U. Time-Resolved Stark Spectroscopy in CdSe Nanoplatelets: Exciton Binding Energy, Polarizability, and Field-Dependent Radiative Rates. *Nano Lett.* **2016**, *16* (10), 6576–6583. https://doi.org/10.1021/acs.nanolett.6b03244.
(46) Xie, S.; Zhu, H.; Li, M.; Bulović, V. Voltage-Controlled Reversible Modulation of Colloidal Quantum Dot Thin Film Photoluminescence. *Appl. Phys. Lett.* **2022**, *120* (21), 211104. https://doi.org/10.1063/5.0093248.
(47) Konstantatos, G.; Sargent, E. H. PbS Colloidal Quantum Dot Photoconductive Photodetectors: Transport, Traps, and Gain. *Appl. Phys. Lett.* **2007**, *91* (17), 173505. https://doi.org/10.1063/1.2800805.
(48) Liu, H.; Lhuillier, E.; Guyot-Sionnest, P. 1/f Noise in Semiconductor and Metal Nanocrystal Solids. *J. Appl. Phys.* **2014**, *115* (15), 154309. https://doi.org/10.1063/1.4871682.
(49) Geremew, A.; Qian, C.; Abelson, A.; Rumyantsev, S.; Kargar, F.; Law, M.; Balandin, A. A. Low-Frequency Electronic Noise in Superlattice and Random-Packed Thin Films of Colloidal Quantum Dots. *Nanoscale* **2019**, *11* (42), 20171–20178. https://doi.org/10.1039/C9NR06899F.
(50) Palaferri, D.; Todorov, Y.; Bigioli, A.; Mottaghizadeh, A.; Gacemi, D.; Calabrese, A.; Vasanelli, A.; Li, L.; Davies, A. G.; Linfield, E. H.; Kapsalidis, F.; Beck, M.; Faist, J.; Sirtori, C. Room-Temperature Nine-Mm-Wavelength Photodetectors and GHz-Frequency Heterodyne Receivers. *Nature* **2018**, *556* (7699), 85–88. https://doi.org/10.1038/nature25790.

TOC graphic

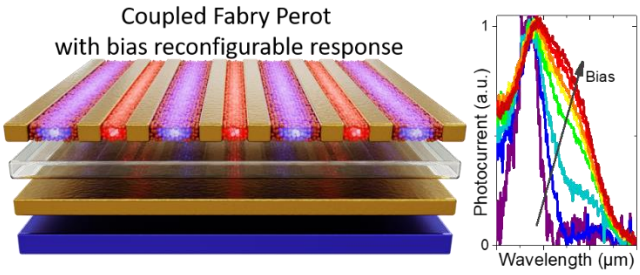
Coupled Fabry Perot
with bias reconfigurable response
Photocurrent (a.u.)
1
0
Bias
Wavelength (μm)